Case Studies in Thermal Engineering 54 (2024) 104087

Contents lists available at ScienceDirect

Case Studies in Thermal Engineering

journal homepage: www.elsevier.com/locate/csite

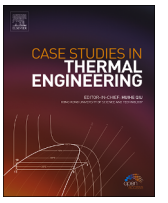

Artificial intelligence-assisted characterization and optimization of red mud-based nanofluids for high-efficiency direct solar thermal absorption

K. Praveen Kumar [a, **], Rohit Khedkar [b, ***], Prabhakar Sharma [c, ****], Rajvikram Madurai Elavarasan [d], Prabhu Paramasivam [e], V. Vicki Wanatasanappan [a, *****], Sesathiri Dhanasekaran [f, *]

[a] Institute of Power Engineering, Universiti Tenaga Nasional, Jalan IKRAM-UNITEN, 43000, Selangor, Malaysia
[b] Department of Chemical Engineering, School of Engineering, P P Savani University, Surat, 395009, Gujarat, India
[c] Department of Mechanical Engineering, Delhi Skill and Entrepreneurship University, Delhi, 110089, India
[d] Research and Development Division, Nestlives Private Limited, Chennai, 600091, India
[e] Department of Research and Innovation, Saveetha School of Engineering, SIMATS, Chennai, Tamilnadu, 602105, India
[f] Department of Computer Science, UiT The Arctic University of Norway, Tromso, Norway

* Corresponding author.
** Corresponding author.
*** Corresponding author.
**** Corresponding author.
***** Corresponding author.
E-mail address: seshathiri.dhanasekaran@uit.no (S. Dhanasekaran).

https://doi.org/10.1016/j.csite.2024.104087
Received 22 July 2023; Received in revised form 26 January 2024; Accepted 29 January 2024
Available online 30 January 2024

GRAPHICAL ABSTRACT

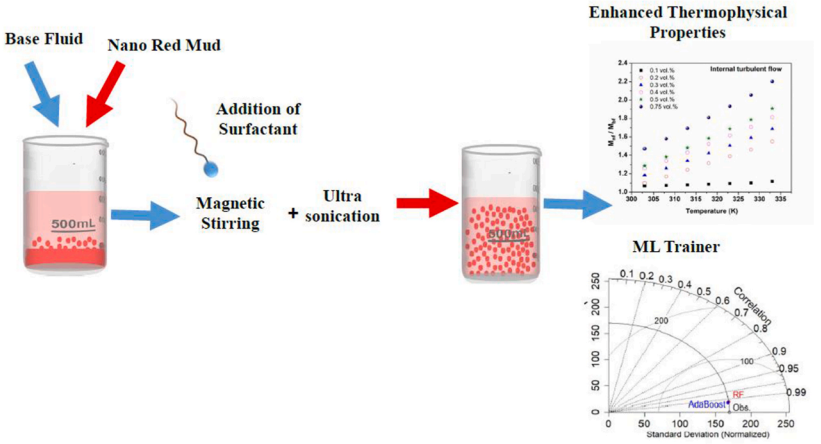

ARTICLE INFO

Keywords:
Machine learning
Red mud
Solar energy
Specific heat
Thermal properties
Waste material

ABSTRACT

The utilization of nanofluids (NFs) holds promise for enhancing the thermal efficiency of solar thermal collectors. Among the various NF solutions, red mud (RM) NFs have gained attention due to their effective absorption of solar thermal energy. RM comprises precious metal oxides, making it a proficient medium for direct solar heat absorption. This study aimed to formulate water-based RM NFs with concentrations ranging from 0.1 to 0.75 vol%. Within the temperature range of 303–333 K, we assessed the specific heat (SH), viscosity (VST), and thermal conductivity (TC) of the NFs. To maintain stability, we employed polyvinylpyrrolidone (PVP) surfactant. The results indicated that the SH of RM NFs is lower than that of water. Additionally, as RM NF concentrations increased, there was a significant improvement in TC. The highest TC enhancement of 36.9 % is observed at 333 K for a concentration of 0.75 vol% compared to water. Based on the gathered data, unique equations were developed to estimate the properties of RM NFs within the studied range. Our findings suggest that RM NFs have the potential to effectively replace water in solar energy applications. Furthermore, we employed innovative ensemble-type machine learning (ML) techniques, namely Adaptive Boosting (AdaBoost) and random forest (RF), to address the problem. We also utilized these novel ML methods to construct metamodels for predicting the considered properties, offering accurate and efficient models for analyzing NF behavior. The incorporation of RM in solar thermal applications could contribute to resolving disposal challenges associated with this waste material, thereby aiding in its long-term management.

1. Introduction

Over the last decade, NFs have undergone significant advancements, emerging as highly effective working fluids in solar energy conversion to address the growing global energy demand. Ongoing research focuses on exploring the long-term stability, thermophysical properties, and rheology of NFs, aiming to facilitate their successful application in sustainable solar collectors. While many researchers have predominantly utilized NFs crafted from conventional metal oxides, metallic materials, or carbon nanoparticles (NPs), attention is shifting towards alternative sources, particularly industrial waste products like RM, which predominantly consist of valuable metal oxides.

The backdrop of these technological developments is set against the backdrop of global urbanization and industrialization. While these processes are essential for societal progress, their negative impacts on the global ecology and social well-being cannot be overlooked. A primary concern arising from these global operations is the generation of substantial amounts of industrial waste, accompanied by challenges related to its safe management and disposal. A secondary challenge is the scarcity of available land, resources, and assets, posing constraints on continued infrastructure development [1,2].

The production of alumina gives rise to a solid industrial by-product known as RM. Its distinctive red color is attributed to a significant content of iron oxide. The type of bauxite utilized for alumina extraction and the manufacturing process plays a direct role in determining the quantity of RM generated. Typically, the production of RM from the extraction of one ton of alumina exceeds 1.5 tons.

Projections suggest an annual output of approximately 150 million tons of RM, contributing to a global stockpile surpassing 4.6 billion tons [1,2].

Traditionally, RM has been disposed of by dumping it into the sea or landfills, posing environmental hazards by contaminating soil, water, and air in the surrounding areas. Recognizing the environmental concerns associated with RM disposal, there is a growing emphasis on efficient recycling. RM, owing to its composition primarily comprising metal oxides along with trace amounts of Silica, Calcium, and Sodium, holds potential for various applications. Its reuse can involve serving as a substitute material or facilitating the recovery of metals [3,4]. Additionally, the iron-rich phases in RM, contributing to its red coloration, make it suitable for use as a dye. There is a significant push for large-scale reprocessing of RM, aiming to establish further practical applications. Notably, the prospect of employing RM as a building material has garnered increased attention [5].

Reducing the emissions of the principal greenhouse gas responsible for global warming and climate change is crucial. The swift expansion of sustainable and environmentally friendly sources of renewable energy is evident [6]. One widely utilized renewable energy source is solar energy, harnessed from the sun's radiant light and heat. Various technologies, including photovoltaic thermal systems, are employed to capture and convert solar energy into electricity [7]. The use of thermal energy storage technology enables the generation of electrical power as needed, not only during the day but also at night. Thermal energy storage has gained increased attractiveness due to its cost-effectiveness, enhanced thermal power conversion efficiency, environmental friendliness, and efficient energy storage capabilities [8].

NFs represent a distinctive class of fluids formed by dispersing nanoscale particles (1–100 nm) within a conventional base fluid [9]. The term "NF" was officially coined by Choi in 1995 to describe fluids containing particles within the 1–100 nm range [10]. Traditional heat transport fluids like oil, water, paraffin, acetone, and ethylene glycol exhibit limited heat transmission capabilities, prompting scientists to conduct numerous experiments aiming to enhance their heat transfer rates by augmenting their TC through the addition of NPs [11]. It is imperative to enhance thermal system efficiency and promote energy conservation. An increase in TC not only enhances efficiency but also accelerates cooling processes while reducing overall energy consumption. Optimal selection of the base fluid and NPs can significantly enhance the overall effectiveness of thermal systems. Typically, metals and their oxides, carbides, or carbon nanotubes serve as NPs in NFs. The unique characteristics of NFs render them potentially advantageous in various heat transfer applications, spanning batteries, heat exchangers, hydrogen storage reactors, microelectronics, fuel cells, lubrication, pharmacy, and more. The thermophysical properties of NFs are notably influenced by the preparation method employed [11,12]. In contemporary practices, researchers often prefer the two-step method over the one-step method due to the commercial availability of NPs in liquid or powder form, making this approach increasingly prevalent [12,13].

Recent studies have shown that enhancing the thermal properties of NFs involves dispersing NPs derived from fruits, plants, and waste materials into the base liquid [13]. Ranjbarzadeh et al. [14] investigated water-based NFs by incorporating SiO_2 NPs synthesized from rice husk. Sadri et al. [15] introduced an environmentally friendly approach using clove buds to covalently functionalize multi-walled carbon nanotubes and study their heat transport in a heat exchanger. Nune et al. [16] achieved stability in NFs by synthesizing gold NPs through the combination of Au ions with Darjeeling tea leaves. Stephen and Seethalakshmi [17] utilized hesperidin, predominantly obtained from citrus fruits, in conjunction with $AgNO_3$ to create silver NFs. In a small heat exchanger, Bahiraei et al. [18] explored the performance and hydraulic properties of environmentally friendly silver NFs produced through the biological synthesis of silver NPs, utilizing green tea leaf extract as a reducing agent.

Extensive research has been conducted to investigate the factors influencing the TC and VST of NFs produced through the utilization of commercially available NPs or a chemical synthesis approach [19]. However, there is a notable scarcity of studies focused on the environmentally responsible production of NFs. Kontala et al. [19] demonstrated the significance of incorporating RM in the fabrication of hydroelectric cells, marking a noteworthy advancement. The chemical composition of RM is largely contingent on the type of bauxite ore and the various processes involved in alumina manufacturing. Fly ash, a byproduct of coal power plants, shares similar metal oxide compositions with RM. Kanti et al. [20] presented findings on the thermal properties of NFs derived from fly ash and a hybrid of fly ash and copper (Cu). Their conclusion indicated that the developed NFs exhibit superior thermal properties compared to water. Additionally, Kanti et al. [21,22] investigated the heat transfer capabilities of the mentioned NFs across different operational ranges. Their observations underscored the advantageous role of these fluids in heat transfer relative to water.

Sofiah et al. [23] conducted a comprehensive review outlining the diverse thermal properties of NFs in their research paper. Meanwhile, Aslfattahi et al. [24–26] investigated and established the thermal properties of NFs based on different base fluids containing MXene for applications in green energy. Anagnostopoulos et al. [27] observed that by milling nitrate salts together with RM and subsequently compressing and sintering the resulting mixture, composite phase change materials (CPCMs) can be developed. This innovative CPCM demonstrates exceptional performance over a temperature range of 25–400 °C, providing an effective solution for recovering waste heat from medium to high-temperature streams. Not only does this approach offer a valuable avenue for waste heat recovery, but it also presents an opportunity to vaporize RM as a by-product for energy-related applications. Wang et al. [28] introduced a novel solar absorber with reduced RM content, showcasing favorable light absorption and photothermal conversion capabilities achieved through biomass pyrolysis. When integrated into a substrate of polyvinyl alcohol and chitosan gel, the absorber achieves an impressive light absorptance of 94.7 %. In a study by Sertkaya and Canli [29], the impact of red mud on the cooling performance as a heat transfer fluid was investigated. Their findings suggest that incorporating 9 wt% water-based RM NF can reduce the cooling period by approximately 14 s compared to the base fluid.

The examination of the literature reveals that RM, containing valuable metal oxides in varying mass ratios, has been transformed into RM NF. This involves the integration of nano-sized RM particles into a fluid, typically water or another base fluid, and has been the subject of diverse studies due to its distinctive properties and potential advantages. RM NF exhibits promise for a range of applications, including serving as heat transfer fluids, enhancing solar absorbers, contributing to phase change materials, facilitating cooling

processes, and enabling waste heat recovery. It is crucial to emphasize that the effectiveness and appropriateness of RM NF are contingent upon the specific application, the concentration of NPs, and the inherent characteristics of the base fluid.

The novelty of the work is there are no studies on the thermal properties of NFs prepared using RM. This study confirms whether RM is useful in heat transfer applications or not. In this work, micron-sized RM particles were initially ball-milled for 48 h to get a nano size of 21.5 nm. The water base RM NFs were developed in the 0.1–0.75 vol% range. The stability is determined for prepared NFs. The SH, VST, and TC were determined in the 303–333 K temperature range for the defined concentrations of NFs. The prepared RM NPs were characterized by various techniques. Using the obtained data, the correlations were developed for the prepared NFs to estimate the above-mentioned thermal properties. The measured thermal properties determine the heat transfer ability parameter for the studied NF. Finally, AdaBoost and RF, model-prediction techniques effectively simulated the nonlinear and complicated interaction between thermal properties at different temperatures and concentrations of NFs.

2. Experimental procedure

2.1. Materials

Micron-sized RM particles (50 μm) were gathered from the NALCO alumina refinery in Dhamanjodi, Odisha, India. These particles underwent an initial sieving process using the American Society for Testing and Materials (ASTM) 300 mesh. Subsequently, double distilled water was utilized for multiple washes to diminish the alkalinity of the sieved material. The treated particles were then subjected to a ball mill (Model: U-Tech Laboratory Stainless Steel Ball Mill) with a 1 kg jar for 48 h to achieve the necessary nano size. Zirconia balls (20 and 10 mm) within the jar operated at a speed of 200 rpm during this milling process. This treatment led to a substantial increase in the surface area of RM, resulting in a transformation of particles from micro to nanoscale [15]. Table 1 depicts the comparison of RM thermal properties with other NPs.

2.2. Characterization

To analyze the RM NPs, various characterization techniques were employed. Transmission Electron Microscopy (TEM) using a JEOL JEM-2100F model, X-ray Fluorescence (XRF) with a PAN analytical Zetium model, and a Nanoparticle Size Analyzer (Winner 802 DLS model) were utilized. The stability of the NF was assessed based on zeta potential (ZP) values, and this measurement was conducted using a Nano-zeta sizer instrument from Malvern Instruments, UK [22].

2.3. Preparation of nanofluid

The formulation of the RM NF follows a two-step method. The quantity of NPs required to achieve the specified volume concentrations of RM NF is determined using Eq. (1) [21]. The calculated amount of RM NPs needed for each concentration in NF preparation is precisely measured using a digital electrical balance with an accuracy of ±0.0001g (model: WENSAR, MAB220T). These NPs are then dispersed in 100 mL of water. Subsequently, PVP surfactant, constituting 5 % of the NPs' weight for each concentration, is introduced to the solution to enhance the stability of the NFs. To prevent particle agglomeration, the solution undergoes magnetic stirring (Model: REMI MS-800 Plus) and sonication using a Hielscher ultrasonic processor (Model: 200 W, 24 kHz, UP200S) for 30 and 45 min, respectively. Fig. 1 depicts the schematic diagram for the preparation of RM NF.

Table 1
Comparison of red mud thermal properties with other nanoparticles.

Property	Red-mud	SiO_2 [14]	Fe_2O_3 [12]	Al_2O_3 [7]	Fly ash [21]
Density (Kg/m^3)	3260	2200	5950	3890	1920
Thermal conductivity (W/m-k)	11.7	1.4	7	40	1.7
Specific heat (J/kg-K)	1316	745	451	773	745

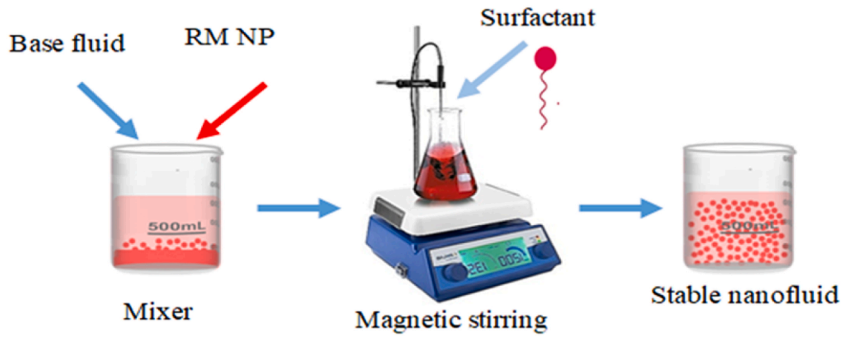

Fig. 1. Schematic diagram for red mud nanofluid preparation. (For interpretation of the references to color in this figure legend, the reader is referred to the Web version of this article.)

$$\varphi_v\,(\%) = \frac{\left(\frac{m_{red\ mud}}{\rho_{red\ mud}}\right)}{\left(\frac{m_{red\ mud}}{\rho_{red\ mud}}\right) + \left(\frac{m_{water}}{\rho_{water}}\right)} \tag{1}$$

Where φ_v is the volume concentration of the NF. $\rho_{red\ mud}$ and ρ_{water} is the density of RM NP and water, respectively. $m_{red\ mud}$ and m_{water} is the mass of RM NP and water, respectively.

2.4. Thermal properties

To assess the SH of the synthesized NFs, a differential scanning calorimeter (Model: SI DSC Japan) was employed with an instrument accuracy of ± 5 %. The authors followed the procedure outlined by O'Hanley et al. [30] for measuring the SH of NFs. The validation of this differential scanning calorimeter process was conducted by initially examining the SH of the base fluid (water) before measuring the NF, and these results were compared with the SH of water available in the American Society of Heating, Refrigerating, and Air-Conditioning Engineers (ASHRAE) data handbook and other literature sources [31].

The VST of the NFs was measured using the Brookfield DV-I PRIME digital viscometer. The instrument was equipped with a temperature bath to maintain the samples' temperature during VST measurements [32]. The instrument has an accuracy of ± 2 % and repeatability of ± 5 % [32,33].

The TC of RM NFs was determined using the KD2 Pro Analyzer from Decagon Devices, USA [22]. The instrument utilizes a KS-1 stainless steel sensor (60 mm long and 1.27 mm in diameter) with a transient line heat source. By employing a small amount of pulsed heat, the device accurately measures the working fluid's TC, minimizing convective heat transfer for precise prediction of conduction heat transfer. The maximum error of the KD2 Pro is ±5 % [33]. TC measurements of NF samples were conducted with the samples immersed in a hot bath at the required steady-state temperatures [32,33]. The properties of the base fluid were evaluated five times at various temperatures before measuring the parameters mentioned above for NFs. A 15-min gap between each subsequent measurement was observed to ensure equilibrium [34,35].

2.5. Machine learning methods

2.5.1. AdaBoost

AdaBoost is an ensemble strategy for improving weak estimators to build a stronger and more accurate regressor for process prediction. While using this method, a regressor is first fitted to the primary data values. Afterward, further copies of the regressor are fitted to the same data, but their weights are changed depending on how well the current prediction worked out [36,37]. Its core concept is to combine weak learners to generate strong learners. During the AdaBoost algorithm's training phase, every weak learner is loaded with a weight depending on the rate of accuracy, and the weight is allocated to each sample employed in training, indicating the precision of the model training process. If any training samples are properly categorized, the weight will be lowered while a weak learner is added [38,39]. The architecture of AdaBoost methods can be described as:

For a training dataset 'Z' such as $Z = \{(x_1,y_1),\ldots\ldots,(x_n,y_n)\}$, the input vector being x_n, objective vector being y_n and the total number of data points is n. The weighted vectors are assigned as: $w_i(x_i) = 1/n$ in case $i = 1,2,3,\ldots,n.$, for L weak learners, $R_l\left(l = 1.2.3,\ldots\ldots,L\right.$. The rate of residuals is estimated as [40,41];

$$\in_p = \sum P_l\,(x_i)\,\left[R_l\,(x_i) - \,(y_i)\right]; \tag{2}$$

$$\text{Where, } P_l\,(x_i) = \frac{w_t\,(x_i)}{\sum_{i=1}^{n} w_t\,(x_i)} \text{ within } \in_p > 0.5 \tag{3}$$

The weight bias can be estimated using:

$$\beta_l = \log\left(\frac{\in_p}{1 - \in_p}\right) \tag{4}$$

Weight adjustment can then be applied to all training data from 'i' to 'n' in the following stage:

$$w_{t+1}\,(x_i) = w_t\,(x_i) \times e^{-y_i\,R_l(x_i)\beta_l}; \tag{5}$$

where $\in_p > 0.001$ leads to an estimation of $P_l(x_i)$.

It results in combining several weak learners with stringer learners.

$$R\,(x) = sign\left[\sum_{j}^{L} \beta_l\ \left[R_l\,(x) = y\right]\right] \tag{6}$$

The Bayesian ridge regression (BRR) is employed as the base model. BRR is a Bayesian approach that assumes all regression results have identical variance. As a result, all markers with similar genotype frequency describe the same fraction of the additive eccentricities and have the same contraction impact in an additive model. Fig. 2 (a) presents the AdaBoost technique flow chart. The procedure published by Guelman [42] for AdaBoost was followed in this work.

2.5.2. Random forest

RF is a meta-learner technique, meaning that it is composed of several unitary learners, also referred to as decision trees. It can be used for both classifications as well as regression. RF is primarily a bagging method, not a boosting method. Random sampling with replacement is referred to as bootstrapping [43]. The bootstrap method helps us better understand the data set's bias and volatility. Bootstrapping entails randomly picking a small part of the data collection. To reduce the variance of high-variance algorithms like decision trees, a general strategy called bagging may be applied. Bagging enables the independent execution of each model before the

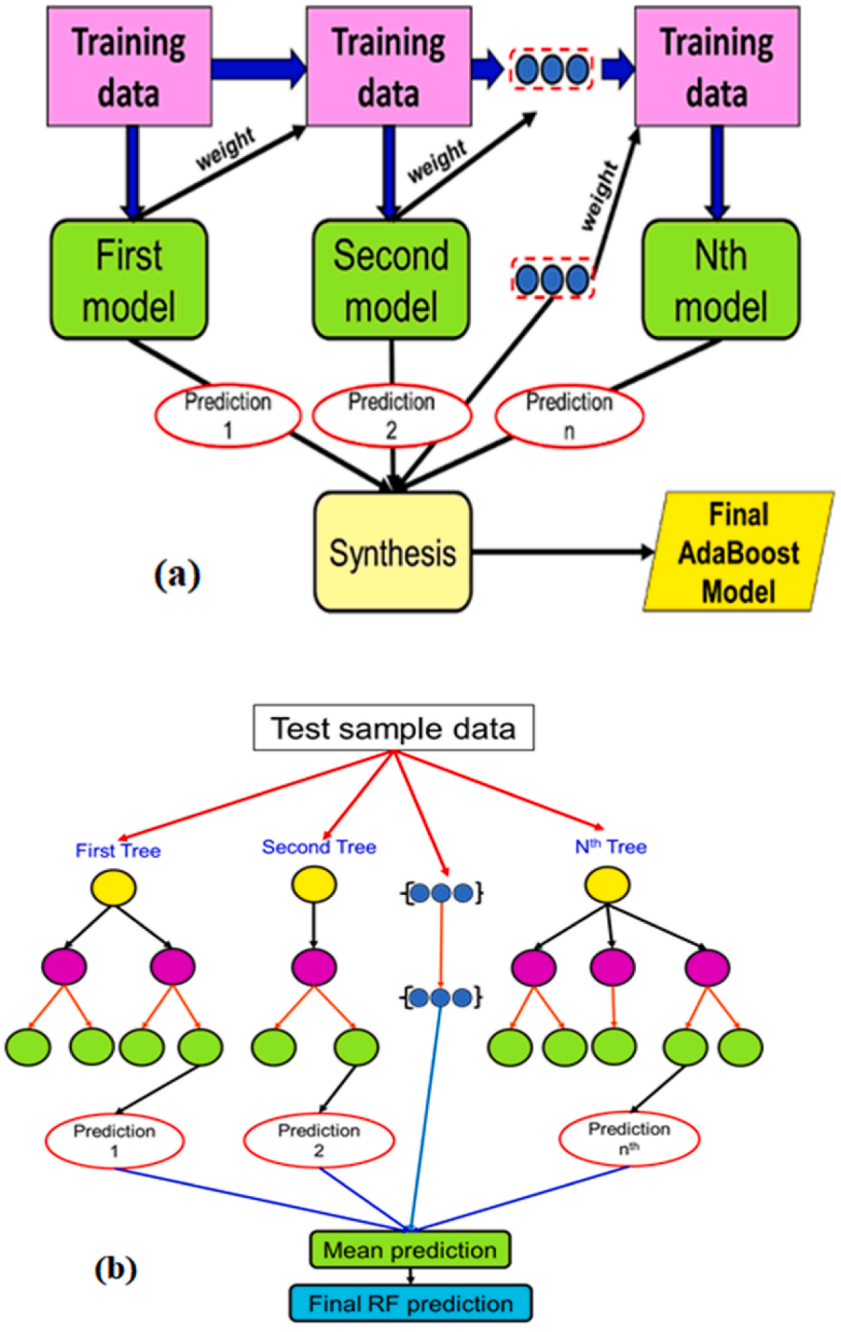

Fig. 2. Flow chart for (a) AdaBoost (b) Random Forest.

model-neutral aggregation of the results. The trees in random forests operate in parallel, which means there is no contact between these trees while they are being built [44]. Fig. 2 (b) presents the RF technique flow chart.

This work used Python-based libraries to execute the RF, and the RF regressor approach is used to forecast the thermo-physical characteristics of NFs, notably TC, SH, and VST. Using the data gathered during the experimental research, the prediction models were created. 30 % of the data points are assigned for prediction and model evaluation, and the remaining 70 % are assigned as a training dataset for building RF models [45]. The RF regressor model was optimized using the input parameters, such as the quantity of trees or leaf nodes. Data points were randomly divided in a 70:30 ratio to the training and testing datasets. Afterward, an RF-based framework was created using the bagging technique and the training dataset, and each model was assessed using a variety of statistical criteria. If the RF model performs poorly, it needs to be optimized, and the expected accuracy must be tested again. After confirming that the model predictive error is within a tolerable range, the accepted model will be used to predict and evaluate the testing dataset [46,47].

2.6. Error evaluation

A battery of statistical evaluations to measure model precision was employed in the present investigation. The correlation coefficient (R) and correlation determinant (R^2) were used to measure the closeness of observed and model-predicted values [45]. Preferably the value of R/R^2 should be close to 1. The root mean squared error (RMSE) was used to measure the prediction error. In recent times, the Kling-Gupta efficiency (KGE), which combines the three components of model errors (bias, correlation, variance ratio, or coefficients of variation) in a more balanced manner, has been widely used for calibration and evaluation of NF's thermophysical models [46]. The following expression was used to measure the statistical indices:

$$R = \frac{\sum_{i=1}^{n} \left(x_a - x_m\right)\left(x_p - y_m\right)}{\sqrt{\sum_{i=1}^{n} \left(x_a - x_m\right)^2}\sqrt{\sum_{i=1}^{n} \left(x_p - y_m\right)^2}} \tag{7}$$

$$MAPE = \frac{1}{n}\sum_{i=1}^{n}\left|\frac{x_p - x_a}{x_a}\right| \times 100 \tag{8}$$

$$RMSE = \left(\sum_{i=1}^{n} \frac{\left(x_p - x_a\right)^2}{n}\right)^{\frac{1}{2}} \tag{9}$$

$$KGE = 1 - \sqrt{(R-1)^2 + \left(\frac{S_{dp}}{S_{da}} - 1\right)^2 + \left(\frac{y_m}{x_m} - 1\right)^2} \tag{10}$$

Where the total count of terms is denoted by 'n' consideration, 'i' is under evaluation term, 'x_a' is actual value, 'x_p' denotes predicted value, the values 'x_m' and 'y_m' represents the mean of actual and forecasted values, respectively. The 'S_{dp}' 'S_{da}' and denotes the standard deviation of predicted and observed values.

3. Results and discussion

3.1. Characterization

Fig. 3 (a) displays the TEM image of RM NPs. In Fig. 3 (a), it is evident that the RM NPs exhibit a spherical shape without significant agglomeration. Fig. 3 (b) and (c) further illustrate the particle distribution of nano RM and the cumulative size distribution in water, respectively. The size of the NPs was determined using an NP size analyzer (Model: Winner 802 DLS) based on the dynamic light scattering (DLS) principle, revealing an observed size of 21.5 nm. Table 2 provides the general chemical composition of both raw material (RM) and Bayer RM utilized in this study. The analysis reveals that RM consists of various metal oxides in different proportions. The chemical composition of the specific Bayer RM examined in this work was determined using an X-ray Fluorescence (Model: PAN analytical Zetium) spectrometer. RM is predominantly comprised of fine and coarse sand particles. It is important to note that the composition, properties, and phases of RM can vary depending on the type of bauxite and the alumina production process, and these characteristics may undergo changes over time [5]. In the current investigation, Bayer RM NPs are found to contain significant components, with Fe_2O_3, Al_2O_3, and SiO_2 constituting substantial portions. The mass fractions of these components are 34.68, 24.86, and 20.96 %, respectively.

3.2. Stability

The quality of particle dispersion in base liquids significantly influences the stability of NFs, as indicated by their hydrodynamic size distribution. NFs exhibit stability when they possess high absolute ZP values, while those with low absolute ZP values are prone to aggregation. Generally, ZP values falling within the range of 40–60 mV are considered indicative of good stability, and values exceeding 60 mV are deemed to represent outstanding stability. Conversely, an absolute ZP of 30 mV is considered to reflect moderate

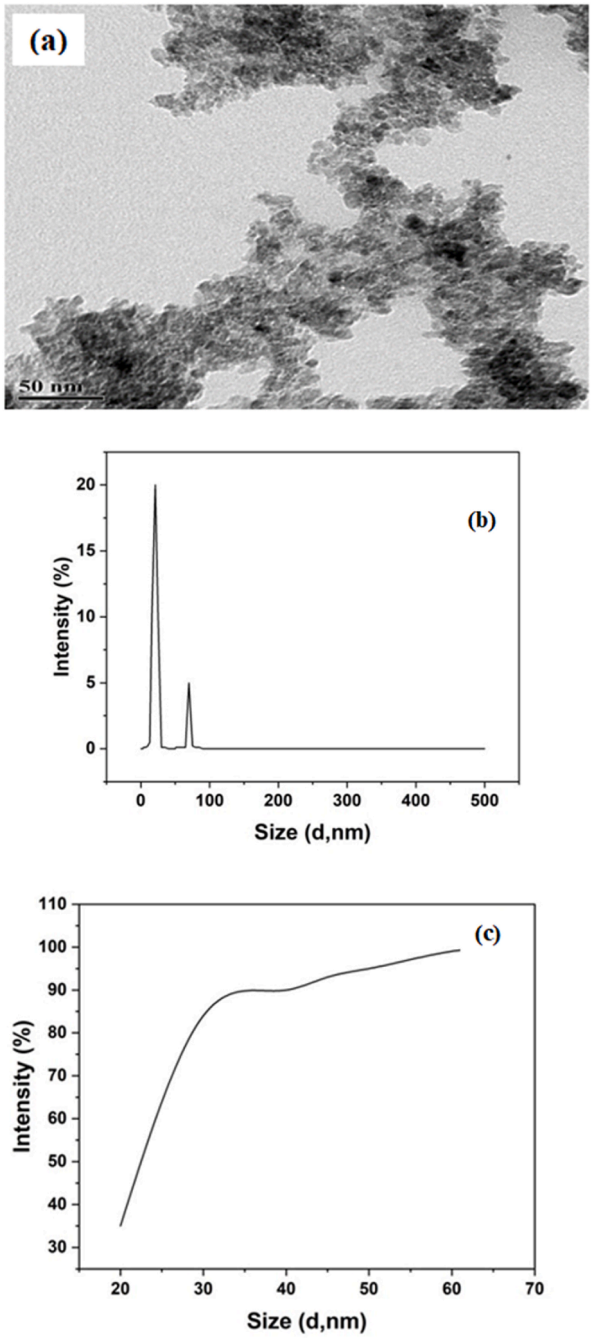

Fig. 3. Red mud nanoparticle (a) TEM image, (b) Distribution, and (c) Cumulative size Distribution.

Table 2
Chemical composition of red mud.

Compounds in mass (%) in grams	Al_2O_3	SiO_2	Fe_2O_3	TiO_2	MgO
General composition of RM [4,5]	20.77	19.41	18.15	4.29	0.62
Bayer red-mud	24.86	20.96	34.68	5.84	1.40

stability, while values below 30 mV are associated with instability. These guidelines help assess and categorize the stability of NFs without compromising their integrity [13,14]. Variables like temperature, pH, surfactant type and quantity, concentration, and ultrasonication frequency and time primarily influence the development of a stable suspension of NF. Generally, NFs exhibit better stability when the pH is away from the isoelectric point [23,48].

The ZP values of the developed NFs were determined using a Nano-zeta sizer (Model: Malvern Instruments, UK). Five separate ZP experiments were carried out at each concentration, and the average values, along with error bars, were employed for the research. Fig. 4 illustrates the ZP values for various concentrations of RM NF, both immediately after preparation and 15 days post-preparation. The results show that the ZP values measured immediately after preparation are higher than those observed after 15 days, indicating an increase in particle agglomeration. This phenomenon is attributed to robust Van der Waals attractive forces between the particles, underscoring the stability of the NFs [48]. However, it is noteworthy that the ZP of the RM NF remains consistently greater than 30 mV across the entire range of test concentrations for more than 15 days after synthesis. This finding confirms the excellent stability of the RM NF, even with the observed increase in particle agglomeration over time.

3.3. Validation

Initially, the SH, VST, and TC of water were determined. Each attribute underwent five tests at various temperatures, and the mean values were utilized for the study. The obtained results were compared with ASHRAE data [31] and findings from other researchers [32,48] to assess the precision of the measuring instruments in capturing thermal properties. Fig. 5 (a) to (c) depicts the validation of water characteristics against ASHRAE [31] and other researchers' data [32,48] within the temperature range of 303–333 K. The comparison reveals no significant deviation between the collected data and the references, indicating a high level of accuracy in the thermal properties measuring tools. Therefore, the instruments are considered to be highly reliable for assessing these properties.

3.4. Thermophysical properties

3.4.1. Specific heat

Fig. 6 (a) depicts the changes in SH values of NF against temperatures at different concentrations of RM NFs. The SH of NF considerably drops at higher concentrations. It is attributed to the RM NPs' SH being significantly less compared to the water and the density at those concentrations and temperatures [49,50]. SH of NF enhances in sync with the temperature at a constant concentration. This shows how temperature affects the NPs' crystal lattice when they are disseminated in the water. With increasing temperature, the thermal fluctuations of the NPs' lattice structure increase [49,50].

Furthermore, the augmentation of NF-SH is attributed to decreased density and improved transport properties [49]. At lower temperatures and greater concentrations, SH amplification is less significant than it is at higher temperatures and lower concentrations. The base fluid water's SH is decreased by the addition of RM NPs [49,50]. The maximum and minimum reduction in the SH of base fluid is 31.2 and 7.93 % for the concentrations of 0.75 and 0.1 vol%, respectively, at 303 and 333 K.

Fig. 6 (b) compares the SH outcomes of RM NFs with those of fly ash NFs, as both materials are considered composite materials comprising various metal oxides in their chemical composition [21]. It is noted that the SH of NFs decreases with concentration but increases with rising temperatures. Across all investigated concentrations and temperatures, the SH of RM NFs is consistently lower than that of fly ash NFs. This distinction can be ascribed to the lower SH of individual metal oxides constituting the RM NPs, as outlined in Tables 1 and 2

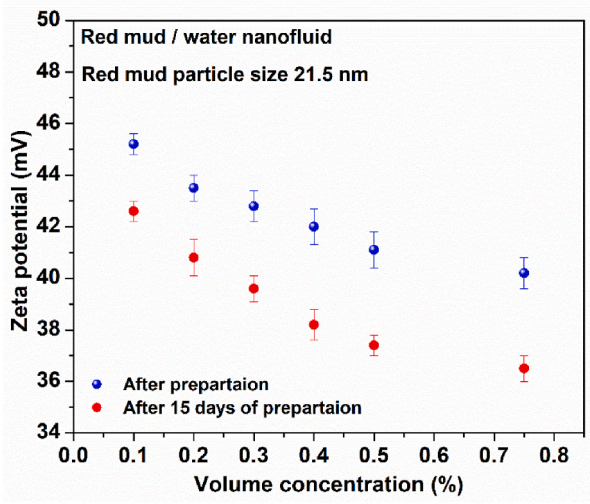

Fig. 4. Zeta potential of red mud nanofluids. (For interpretation of the references to color in this figure legend, the reader is referred to the Web version of this article.)

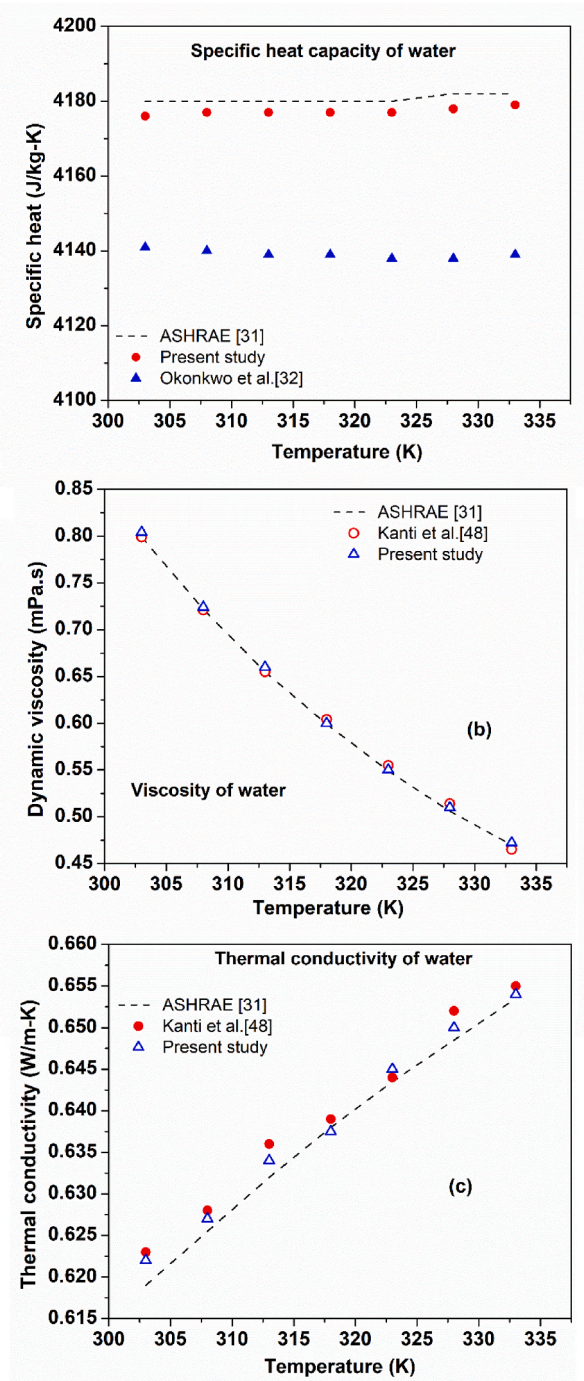

Fig. 5. Comparison of water's (a) specific heat, (b) Viscosity, and (c) Thermal conductivity with ASHRAE [31] data.

3.4.2. Viscosity

Fig. 7 (a) depicts the change in VST values of NF with concentration and temperature. Fig. 7 (a) depicts that the VST of the NFs improves with NP fraction in base liquid when temperature is constant. Increasing concentration means adding more NPs to the base fluid, causing the increase in Van-der Waals forces and NPs adhering. The existence of intermolecular forces between RM NPs brings them together and leads to the clustering effect. The increase of NPs and the formation of aggregates reduce the NP's mobility and increase the friction between the fluid layers and surfaces [21,45]. At a constant temperature of 303K, maximum and minimum amplification in the VST of NF is 18.9 and 2.38 % for the concentration of 0.75 and 0.1 vol%, respectively, relative to water.

Additionally, Fig. 7 (b) shows that at constant concentration, VST decreases with an increase in temperature. It is attributed to the fact that a greater temperature diminishes the effects of intermolecular forces like van der Waals forces and intermolecular bonds,

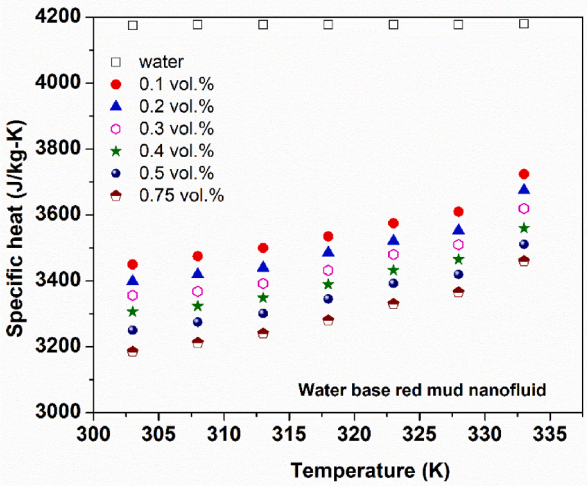

Fig. 6 (a). Variation of specific heat of red mud nanofluid with temperature. (For interpretation of the references to color in this figure legend, the reader is referred to the Web version of this article.)

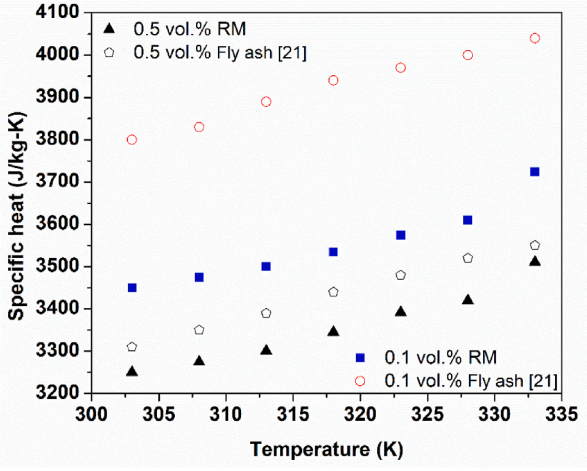

Fig. 6 (b). Comparison of specific heat of red mud nanofluid with fly ash nanofluid [21]. (For interpretation of the references to color in this figure legend, the reader is referred to the Web version of this article.)

which lowers the NF's VST [23]. In other words, decrease in adhesion forces between NPs and the fluid layers with temperature increment. Consequently, increases in NP movement result in a decrease in VST. The maximum and minimum augmentation in the VST of NF is 18.9 and 12.6 % for the concentration of 0.75 % at 303 and 333K, respectively, relative to the base liquid.

Fig. 7 (b) presents the comparison of the VST results of RM NFs with those of fly ash NFs [21]. It is observed that the VST of NFs increases with concentration but decreases with an increase in temperatures. Throughout all studied concentrations and temperatures, the VST of RM NFs consistently surpasses that of fly ash NFs. The possible reasons for this distinction are attributed to factors such as the greater density of RM NPs compared to the density of fly ash NPs presented in Table 1, differences in particle size [12], and the use of surfactants [23].

3.4.3. Thermal conductivity

Fig. 8 (a) illustrates the TC variation with different temperatures and concentrations of NF. The TC improves by increasing the concentration at any temperature [48]. This can be due to the enhanced total surface area of the base liquid with the number of NPs. The ratio of surface to volume of NPs is often extremely greater and is shown to enhance with the decrease in the size of the RM NPs [11–13]. Other possible reasons for the TC enhancement are stochastic and Brownian motion of NPs (21.5 nm), and particle clustering in the base fluid. Furthermore, nano RM NF consists of several metal oxides like hybrid composite NF as observed in Table 1. This is also a possible reason for TC enhancement. The lowest and highest augmentation in the TC of NF is 3.97 and 36.9 % in the case of 0.1 and 0.75 vol% at 333 K, correspondingly, relative to water.

In addition, it is noticed from Fig. 8 (a) that the NF's TC increases with the temperature at a constant concentration. This is because a rise in the temperature of the NFs causes a rise in the random mobility of particles within the liquid and a rise in the NP collision, both of which encourage the augmentation in the TC of NF. Additionally, it can be shown that the TC amplifications are more promi-

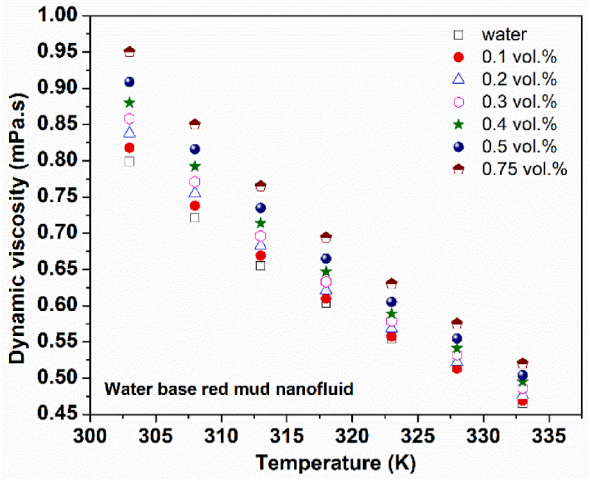

Fig. 7 (a). Variation of viscosity of red mud nanofluid with temperature. (For interpretation of the references to color in this figure legend, the reader is referred to the Web version of this article.)

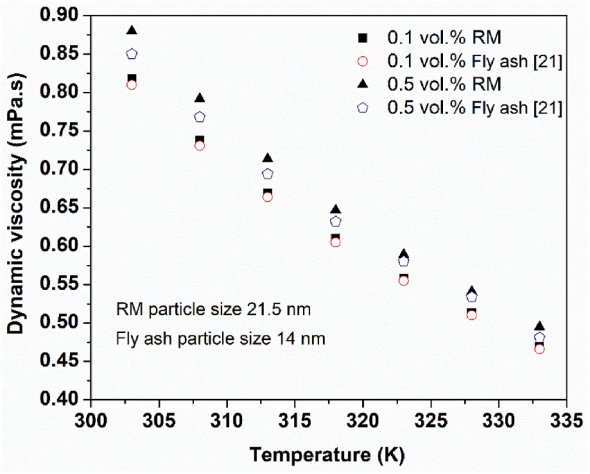

Fig. 7 (b). Comparison of viscosity of red mud nanofluid with fly ash nanofluid data [21]. (For interpretation of the references to color in this figure legend, the reader is referred to the Web version of this article.)

nent at greater temperatures than they are at lower temperatures [14,48]. The maximum and minimum amplification in the TC of NF is 36.9 and 24.7 % for the concentration of 0.75 vol% at 333 and 303 K, respectively relative to the base fluid.

Fig. 8 (b) compares the TC outcomes of RM NFs with those of fly ash NFs [21]. It is noted that the TC of NFs increases with both concentration and temperature. Across all studied concentrations and temperatures, the TC of RM NFs consistently exceeds that of fly ash NFs. The likely explanation for this improvement lies in the chemical composition of RM NPs. In RM NPs, a significant amount of Al_2O_3 and Fe_2O_3 is present, contributing to higher TC values compared to fly ash NPs, where SiO_2 is a significant metal oxide with a lower TC value [21].

3.5. Correlations

Numerous correlations are reported in the literature to determine the various thermal characteristics of different NFs. However, no equations are available to estimate the thermal properties of RM NF in the considered range. The correlations developed to assess the studied properties of NF using determined data are illustrated in Table 3.

Where T_{nf} and T_{ref} are the NF and reference temperatures (273 K), respectively.

3.6. Data analysis

The pre-processing of data is an essential stage in developing a data-driven prognostic model. A comprehensive range of experimental investigations was conducted to gather data on the NF's thermophysical properties. Three different sets of data points were employed, one each for each thermal property. The NF concentration and temperature were the control factors.

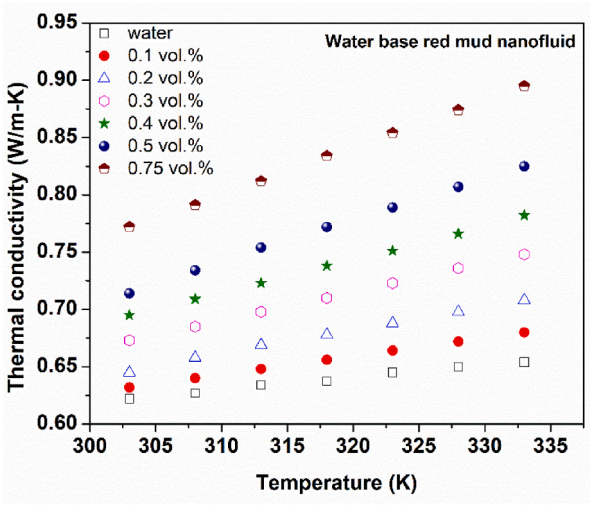

Fig. 8 (a). Variation of thermal conductivity of red mud nanofluid with temperature. (For interpretation of the references to color in this figure legend, the reader is referred to the Web version of this article.)

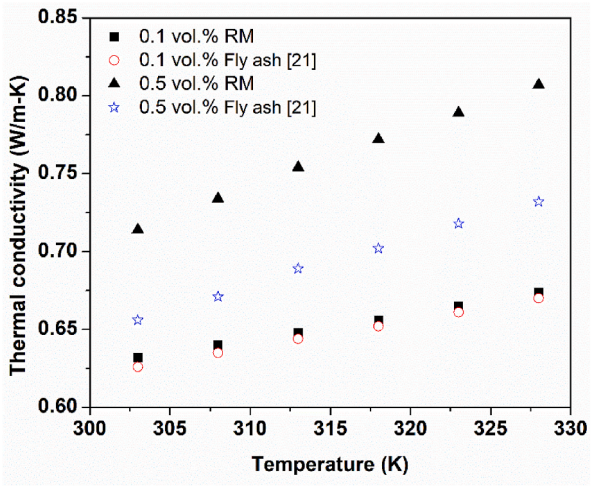

Fig. 8 (b). Comparison of thermal conductivity of red mud nanofluid with fly ash nanofluid [21]. (For interpretation of the references to color in this figure legend, the reader is referred to the Web version of this article.)

Table 3
Developed correlations based on obtained data for RM NF.

Property	Equation	Mean deviation (%)	Standard deviation (%)	Eq. number
Specific heat	$\frac{C_{pnf}}{C_{pbf}} = 0.762^{*}\left(1+\frac{\varphi_v}{100}\right)^{-11.76}{}^{*}\left(\frac{T_{nf}}{T_{ref}}\right)^{0.764}$	0.628	0.763	11
Dynamic viscosity	$\frac{\mu_{nf}}{\mu_{bf}} = 1.066^{*}\left(1+\frac{\varphi_v}{100}\right)^{20.19}{}^{*}\left(\frac{T_{nf}}{T_{ref}}\right)^{-0.466}$	0.634	0.8	12
Thermal conductivity	$\frac{k_{nf}}{k_{bf}} = 0.903^{*}\left(1+\frac{\varphi_v}{100}\right)^{37.6}{}^{*}\left(\frac{T_{nf}}{T_{ref}}\right)^{0.6254}$	0.81	1.07	13

The correlation heatmaps were created for all the measured properties. Fig. 9 depicts the correlation heatmap for TC, VST, and specific heat (SH), respectively. It is the simplest graphical method to show a correlation between independent input and response output. It can be observed from Fig. 8 that the relation between TC and NF concentration is the most significant. A high value of R = 0.89 was observed between TC and NF concentrations. Overall, a healthy and positive correlation in the case of TC was observed. The VST correlation heatmap is shown in Fig. 9. In the case of VST, the temperature shows the most significant as well as negative correlation (−0.97), while the concentration shows a positive correlation (0.22), which was expected as per the physics of the problem. The high value of correlation between VST and temperature denotes that a temperature change is highly sensitive to a change in the value of VST. Fig. 9 illustrates the correlation heatmap for the SH of NFs. In this case, the temperature has the most significant and positive connection (0.69), whereas concentration has a negative correlation (−0.69), as expected, given the physics of

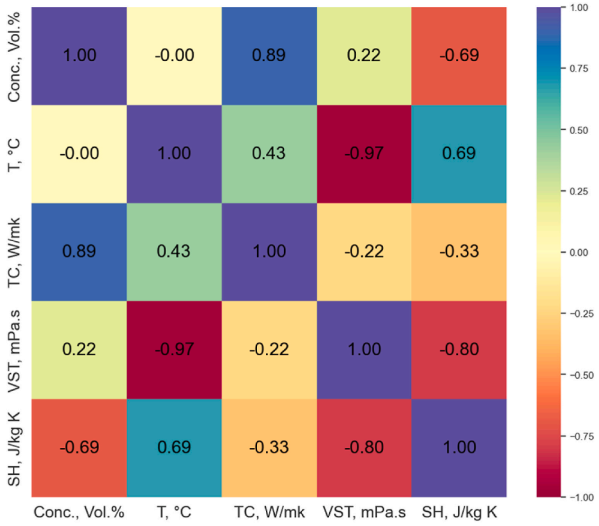

Fig. 9. Correlation heatmap for (a) Thermal conductivity, (b) Viscosity, and (c) Specific heat.

the situation. The significant relationship between SH and temperature indicates that changes in SH are particularly sensitive to changes in temperature [37].

3.7. Predictive model development

This section explores the anticipated outcomes of the two test ML techniques, AdaBoost and RF. A comparative study is used to discover the most successful technique. Temperature and NF volume concentrations were chosen as control factors for the development of a data-driven model. TC, VST, and SH, on the other hand, were chosen as dependent response factors.

3.7.1. Thermal conductivity model

A prediction model was built using the data set acquired through lab-based experiments. The TC values were collected at different parameter ranges of NF's concentration, and temperature. In the first stage, a novel AdaBoost technique was employed to develop the model. The 5-fold cross-validation strategy was used during the model development to minimize the prediction error (MSE) with a short processing time. The 5-fold cross-validation is also an effective approach to prevent model overfitting [47]. The AdaBoost model was then applied to the testing data (30 %) to see how well it performed in generating predictions about unknown data. The developed model was examined based on statistical indices such as R, R^2, RMSE, and KGE. The statistics for the training and testing performance metrics are shown in Table 4. The Preseason's coefficient R was 0.9983 during model training which improved to 0.9993 during the test phase on the unknown data set. The improvement in the 'R-value denotes that the model has not been overtrained. The 'R^2' value for the AdaBoost model was 0.9966 and 0.9986 while the RMSE value was 0.004 and 0.002 during the training and test phases, respectively. The KGE values were estimated to find out the prediction efficiency of the AdaBoost-based TC model. The KGE values for TC models were 0.9961 and 0.9949, respectively.

Fig. 10 (a) depicts a comparison graph of anticipated and observed TC values around the best-fit line during the model training phase while Fig. 10 (b) depicts the same during the test phase. Fig. 10 (c) and (d) show the residuals during the training and test phase. The statistical indices such as KGE, R, and R^2 being close to 1 with low RMSE indicate AdaBoost-based model is a robust prognostic model. The graphical representation showing comparative values and residuals further fortifies the prediction efficacy of the AdaBoost-based TC model [47].

Table 4
Statistical evaluation of prediction models.

Stat. Index	Phase	TC		VST		SH	
		AdaBoost	RF	AdaBoost	RF	AdaBoost	RF
R	Learning	0.9983	0.9934	0.9948	0.9926	0.9938	0.9929
	Testing	0.9993	0.9986	0.9968	0.9953	0.9974	0.9961
R^2	Learning	0.9966	0.9886	0.9896	0.9853	0.9876	0.9859
	Testing	0.9986	0.9973	0.9937	0.9907	0.9948	0.9923
RMSE	Learning	0.004	0.009	0.015	0.018	19.13	20.38
	Testing	0.002	0.003	0.012	0.014	12.36	16.05
KGE	Learning	0.9961	0.9874	0.9891	0.9821	0.9874	0.9867
	Testing	0.9949	0.9843	0.9921	0.9894	0.9879	0.9754

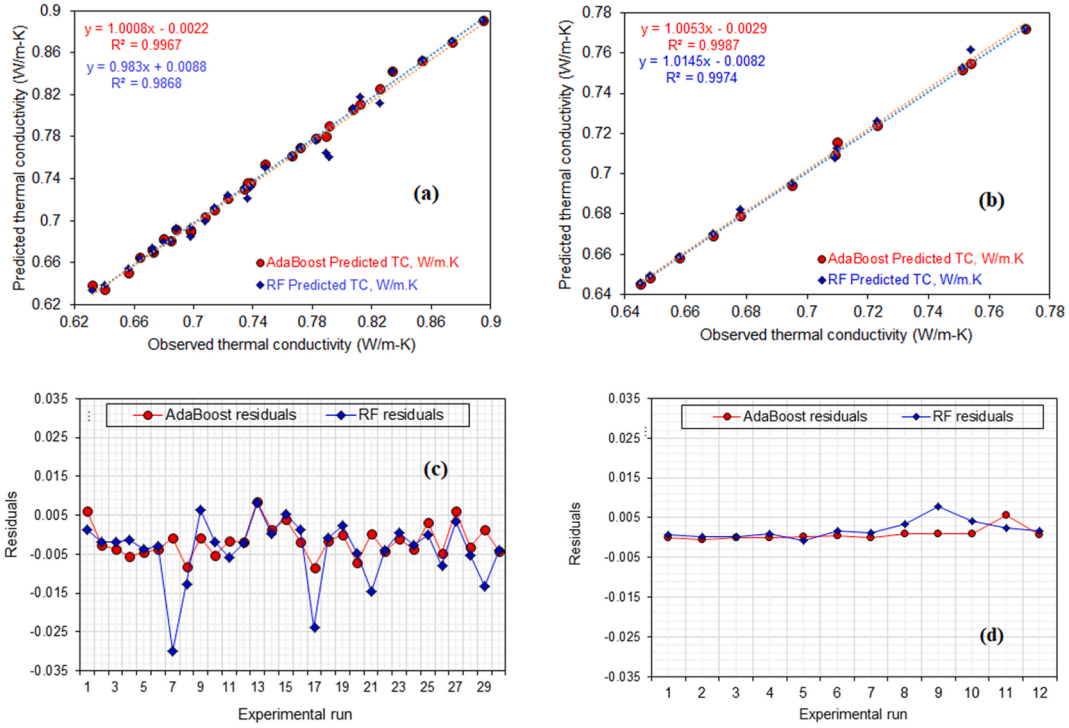

Fig. 10. Thermal conductivity model (a) Observed vs. model predicted during model learning, (b) Observed vs. model predicted during model testing, (c) Residuals during model training, and (d) Residuals during model testing.

In the second phase, the random forest was employed to create the prediction model for TC. Statistical indices such as R, R^2, RMSE, and KGE were used to evaluate this model. Table 4 displays the data for the training and testing performance measures. During model training, the Preseason coefficient R was 0.9934, and it increased to 0.9986 during the test phase on an unknown data set. The increase in the 'R' value indicates that the model has not been overtrained. During the training and test phases, the 'R^{2}' value for the RF-based model was 0.9886 and 0.9973, respectively, while the RMSE value was 0.009 and 0.003. The KGE values were calculated to determine the prediction effectiveness of the RF-based TC model. For TC models, the KGE values were 0.9874 and 0.9843, respectively. Fig. 10 (a) shows a comparison graph of expected and observed TC values around the best-fit line during the model training phase, whereas Fig. 10 (b) shows the same during the test phase. Fig. 10 (c) and (d) depict residuals during the training and testing phases. The statistical indices KGE, R, and R^2 are near to one with low RMSE, indicating that the RF-based model is a robust prognostic model [45,46].

3.7.2. Viscosity

Using the data set obtained from lab-based experiments, a prediction model was VST. The VST values were taken at various NF concentrations and temperature parameter ranges. Statistical indices such as R, R^2, RMSE, and KGE were used to evaluate the developed model. Table 4 displays the statistics for the training and testing performance metrics. During model training, the Preseason coefficient R was 0.9948, and it increased to 0.9968 during the test phase on an unknown data set. The increase in the 'R' value indicates that the model has not been overtrained. During the training and test phases, the 'R^{2}' value for the AdaBoost model was 0.9896 and 0.9937, respectively, while the RMSE value was 0.0015 and 0.0012. The KGE values were estimated to find out the prediction efficiency of the AdaBoost-based VST model. The KGE values for VST models were 0.9891 and 0.9921, respectively.

Fig. 11 (a) shows a comparison graph of expected and observed VST values around the best-fit line during the model training phase, while Fig. 11 (b) shows the same during the test phase. Fig. 11 (c) and (d) depict residuals during the training and testing phases. The statistical indices such as KGE, R, and R^2 being close to 1 with low RMSE indicate AdaBoost-based model is a robust prognostic model. The graphical representation of comparative values and residuals strengthens the prediction efficacy of the AdaBoost-based VST model even more [45–47].

In the second phase, the random forest was applied to develop the prediction model for VST. This model was also evaluated using statistical indices such as R, R^2, RMSE, and KGE. The statistics for the training and testing performance metrics are shown in Table 4. The Preseason coefficient R was 0.9926 during model training and grew to 0.9953 during the test phase on an unknown data set. The rise in 'R' suggests that the model has not been overtrained. The RF-based model's 'R^{2}' value was 0.9853 and 0.9907 during the training and testing stages, respectively, while the RMSE value was 0.018 and 0.014. The KGE values were obtained to assess the predictive power of the RF-based VST model. The KGE values for VST models were 0.9821 and 0.9894, respectively. During the model training phase, Fig. 11 (a) shows a comparison graph of expected and observed VST values around the best-fit line, whereas Fig. 11 (b)

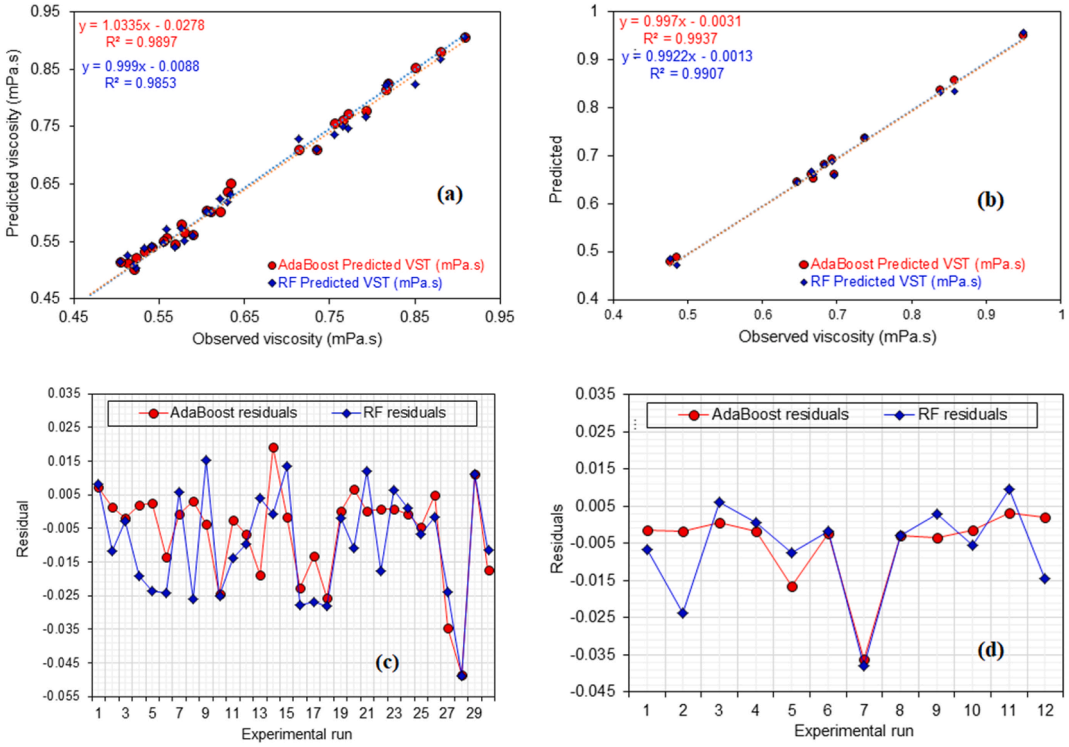

Fig. 11. Viscosity model (a) Observed vs. model predicted during model learning, (b) Observed vs. model predicted during model testing, (c) Residuals during model training, and (d) Residuals during model testing.

shows the same during the test phase. Fig. 11 (c) and (d) depict residuals during the training and testing phases. The statistical indices KGE, R, and R^2 are close to one with low RMSE, showing that the RF-based model is a good predictor.

3.7.3. Specific heat

A SH prediction model was developed using data from lab-based studies. These values were obtained across a wide range of NF concentration and temperature parameters. The constructed model was evaluated using statistical indices such as R, R^2, RMSE, and KGE. The data for the training and testing performance indicators are shown in Table 4. Pearson's coefficient R was 0.9938 during model training and climbed to 0.9974 during the test phase on an unknown data set. The rise in 'R' suggests that the model has not been overtrained. During the training and testing stages, the AdaBoost model's '$R^{2'}$ value was 0.9876 and 0.9948, respectively, while the RMSE value was 19.13 and 12.36. The KGE values were calculated to determine the prediction effectiveness of the AdaBoost-based SH model. For specific models, the KGE values were 0.9874 and 0.9879, respectively.

Fig. 12 (a) depicts a graph comparing anticipated and observed VST values around the best-fit line during the model training phase, whereas Fig. 12 (b) depicts the same during the test phase. Fig. 12 (c) and (d) show residuals throughout the training and testing stages, respectively. The statistical indices KGE, R, and R^2 are near to one with low RMSE, indicating that the AdaBoost-based model is a robust prognostic model. The graphical display of comparison values and residuals establishes the AdaBoost-based SH model's prediction effectiveness even more.

The ensemble RF-based ML techniques were employed to create the prognostic model for SH. The model was used for predictions and statistical indices such as R, R^2, RMSE, and KGE were used to analyze the prognostic capability of the SH model. Table 4 displays the data for the training and testing performance measures. During model training, Pearson's coefficient R was 0.9929, and it increased to 0.9961 during the test phase on an unknown data set. The increase in 'R' indicates that the model was not overtrained. During the training and testing phases, the RF-based model's '$R^{2'}$ value was 0.9859 and 0.9923, respectively, while the RMSE value was 20.38 and 16.05. KGE data were acquired to evaluate the prediction potential of the RF-based SH model. For this model, the KGE values are 0.9867 and 0.9754, respectively. Fig. 12 (a) depicts a comparison graph of anticipated and observed SH values around the best-fit line during the model training phase, while Fig. 12 (b) depicts the same during the test phase. Fig. 12 (c) and (d) show residuals throughout the training and testing stages, respectively. KGE, R, and R^2 are near to one with low RMSE, indicating that the RF-based model is a solid predictor.

3.8. Comparative analysis using Taylor's diagrams

As discussed in previous subsections, both modern ML techniques produced a decent prediction of the thermophysical values of the test NFs over the entire range of test settings. The statistical methods were used to examine the model's correlations, errors, and prediction efficiency as listed in Table 4. It was observed that the outcomes of both techniques were very close to each other. Taylor's

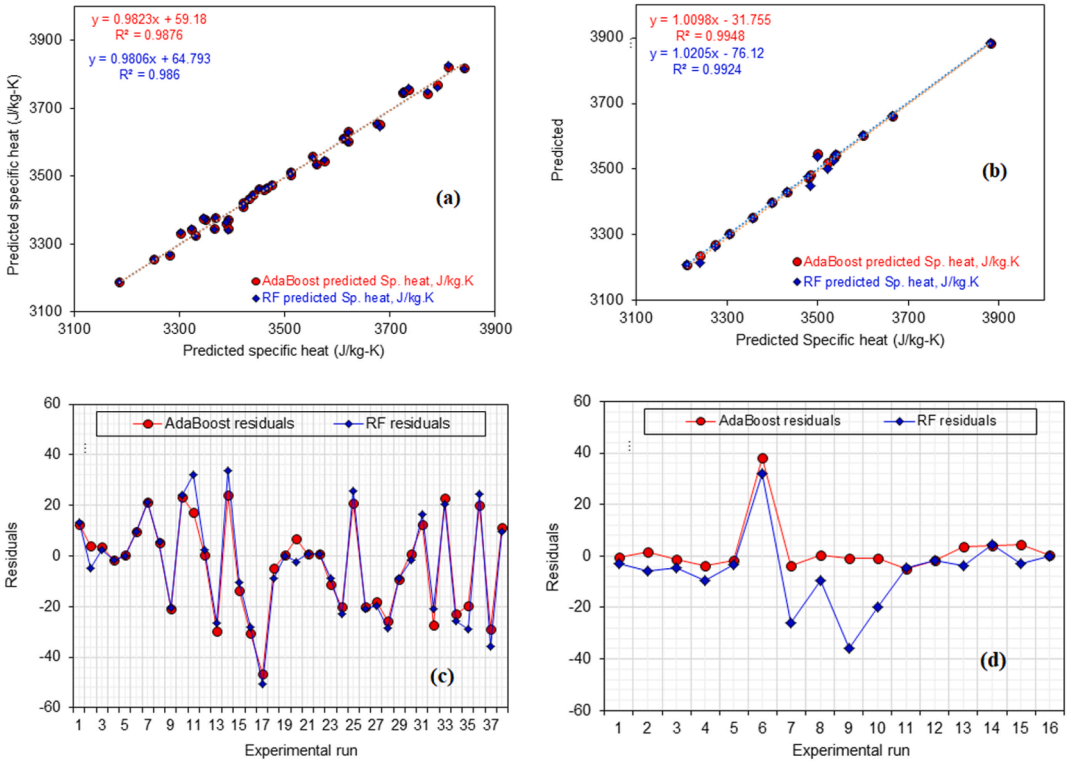

Fig. 12. Specific heat model (a) Observed vs. model predicted during model learning, (b) Observed vs. model predicted during model testing, (c) Residuals during model training, and (d) Residuals during model testing.

diagrams present an excellent way of comparing prediction models. It is a visual graphical representation of inherent model properties for comparison. Taylor's diagrams for all three thermophysical properties are depicted in Fig. 13 (a) to (c). All three of Taylor's diagrams show that the Adaboost-based model's results are marginally superior to the Random forest-based prediction outcomes [45–47].

3.9. Heat transfer ability parameter (HTPA)

Eq. (14), suggested by Prasher et al. [51] used to evaluate NF's heat transfer ability in the internal laminar flow. The relative VST and TC ratio can be used to assess the HTPA. It is intended to determine whether RM NF is advantageous in laminar flow compared to water by employing this HTPA criterion. RM NF will effectively substitute water if the HTPA < 4 for internal laminar flow.

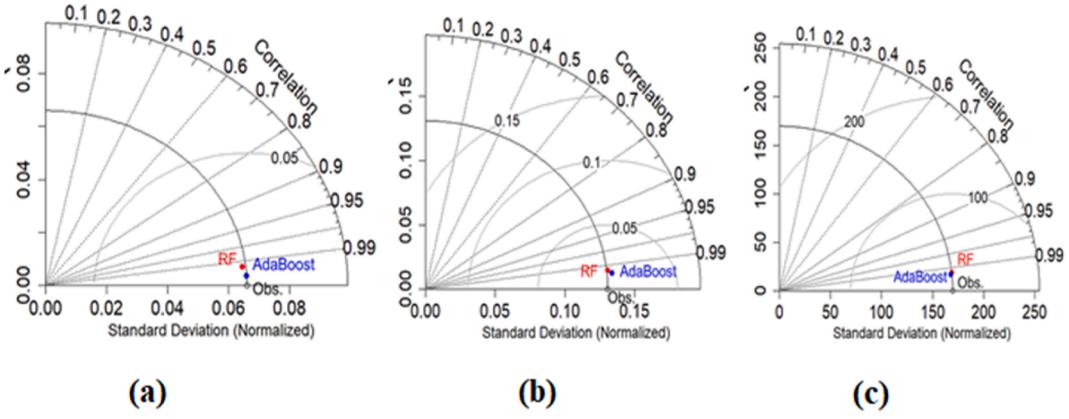

Fig. 13. Taylor's diagram for (a) Thermal conductivity, (b) Viscosity, and (c) Specific heat.

$$\mathrm{HTPA} = \left(\frac{\frac{\mu_{nf}}{\mu_{bf}} - 1}{\frac{k_{nf}}{k_{bf}} - 1} \right) \tag{14}$$

The heat transfer ability parameter calculated using Eq. (14) is less than 4 at all concentrations, as shown in Fig. 14. Therefore, compared to water in an internal laminar flow, considered NFs offer significant advantages in thermal applications.

Mouromtseff number ratio determines the thermal efficiency of various NFs in internal turbulent flow as contrasted to the base fluid. The Mouromtseff value of test NF (M_{nf}) to the Mouromtseff value of the base fluid (M_{bf}) must be greater than 1 for enhanced heat efficiency [52]. For thermal applications, having a higher Mouromtseff number ratio is advantageous. The numerical expression employed to estimate the Mouromtseff number ratio is shown in Eq. (16) [52]. Considering all the fundamental thermal characteristics of RM NF corresponding results were plotted in Fig. 15. The density of RM NF was determined by Eq. (15) based on the law of mixture rule.

$$\rho_{\mathrm{nf}} = \left(1 - \varphi_v\right) \rho_{bf} + \varphi_v \rho_{np} \tag{15}$$

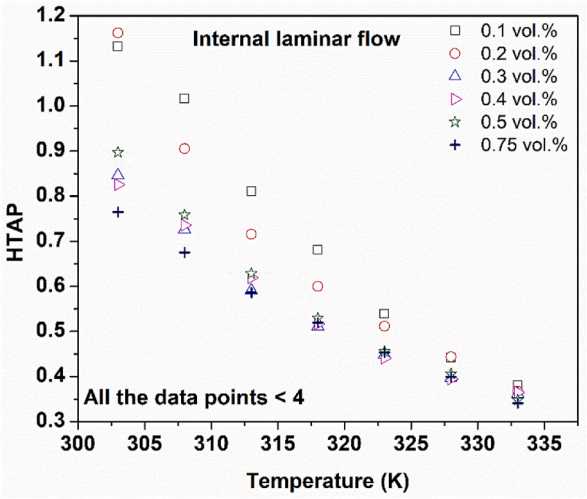

Fig. 14. Heat transfer ability of nanofluid in internal laminar flow.

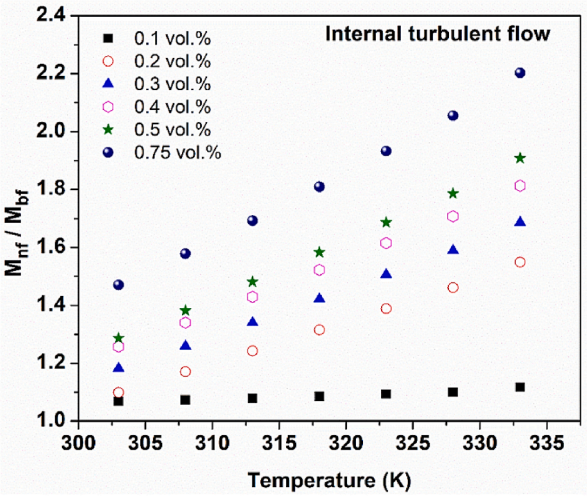

Fig. 15. Internal turbulent flow heat transfer capability of nanofluid.

$$\text{Mouromtseff number } ratio = \frac{\left(\frac{\rho^{0.8}\, k^{0.67}\, c_p^{0.33}}{\mu^{0.47}}\right)_{nanofluid}}{\left(\frac{\rho^{0.8}\, k^{0.67}\, c_p^{0.33}}{\mu^{0.47}}\right)_{base\ fluid}} \tag{16}$$

It can be observed the developed NF provides a Mouromtseff number ratio greater than 1 in the studied range. Hence, this encouraging result establishes RM NF as a promising working fluid for thermal applications.

4. Conclusion

The thermophysical properties of the stable RM NF were measured within the temperature range of 303–333 K, covering concentrations from 0.1 to 0.75 %. Theoretical evaluations are conducted utilizing equations documented in the literature to ascertain the heat transfer capacity of generated NFs in various flow regimes. ML approaches were employed to construct metamodels for the prediction of thermal characteristics. The following are the main results drawn from this study.

1. The ball milling time of 48 h is required to reduce the size of 48 μm to 21.5 nm.
2. RM NF has a lower specific heat than water because of an inherent property of RM NPs. The peak reduction in water's specific heat was 31.2 %, in the case when a concentration of 0.75 vol%, at 303K.
3. VST of RM NF increases with concentration and reduces with temperature. The highest and lowest VST augmentation of RM NF is 18.9 and 1.52 % at 303 and 333K for a concentration of 0.75 and 0.1 vol% relative to water.
4. The maximum and minimum amplification in the TC of NF is 36.9 and 24.7 % for the concentration of 0.75 vol% at 333 and 303 K, respectively relative to the base fluid.
5. The chemical composition and smaller particle size of RM NP contribute to the TC enhancement of RM NF. Theoretical assessment of the heat transfer ability of NFs shows that developed NFs are beneficial in both laminar and turbulent flows.
6. AdaBoost (R = 0.9938–0.9983, R^2 = 0.9937–0.9986) was superior to random forest-based regression (R = 0.9926–0.9983, R^2 = 0.9937–0.9986).
7. The Kling Gupta efficiency also demonstrates that AdaBoost's prediction efficiency (0.9879–0.9949) was superior to RF (0.9754–0.9894).

The present study results show that RM NFs is beneficial as a coolant fluid due to its chemical composition in green energy applications like solar energy. However, further research is needed to optimize the NP concentration, investigate the long-term stability, and compare their performance with other types of NPs as well as in other base fluids.

CRediT authorship contribution statement

K. Praveen Kumar: Software, Project administration, Formal analysis, Data curation. **Rohit Khedkar:** Writing – review & editing, Writing – original draft, Formal analysis, Data curation, Conceptualization. **Prabhakar Sharma:** Resources, Methodology, Investigation. **Rajvikram Madurai Elavarasan:** Visualization, Investigation. **Prabhu Paramasivam:** Supervision, Software, Resources. **V. Vicki Wanatasanappan:** Conceptualization, Data curation, Visualization. **Sesathiri Dhanasekaran:** Writing – review & editing, Visualization, Validation, Resources, Project administration, Data curation, Conceptualization.

Declaration of competing interest

The authors declare that they have no known competing financial interests or personal relationships that could have appeared to influence the work reported in this paper.

Data availability

Data will be made available on request.

Acknowledgements

The authors extend their appreciation to the Deanship of Scientific Research at King Khalid University for funding this work through large group research project under grant number RGP2/7/44.

Nomenclature

C_p	: specific heat (J/kg − K)
k	thermal conductivity (W/m-K)
R	correlation coefficient
R^2	correlation determinant
T	temperature (K)

Greek symbols

ρ	density (kg/m^3)
φ_v:	Volume concentration
μ	viscosity (mPa.s)

Subscripts

bf	base fluid
nf	nanofluid

References

[1] K. Deelwal, K. Dharavath, M. Kulshreshtha, Evaluation OF CHARACTERISTIC properties OF red mud for possible use as a geotechnical material in civil construction, Int. J. Adv. Eng. Technol. 7 (2014) 1053–1059.

[2] F. Lyu, S. Niu, L. Wang, R. Liu, W. Sun, D. He, Efficient removal of Pb(II) ions from aqueous solution by modified red mud, J. Hazard Mater. 406 (2021) 124678, https://doi.org/10.1016/j.jhazmat.2020.124678.

[3] Z. Gong, J. Ma, D. Wang, S. Niu, B. Yan, Q. Shi, et al., Insights into modified red mud for the selective catalytic reduction of NO : activation mechanism of targeted leaching, J. Hazard Mater. 394 (2020) 122536, https://doi.org/10.1016/j.jhazmat.2020.122536.

[4] X. Liu, Y. Han, F. He, P. Gao, S. Yuan, Characteristic, hazard and iron recovery technology of red mud - a critical review, J. Hazard Mater. 420 (2021) 126542, https://doi.org/10.1016/j.jhazmat.2021.126542.

[5] P. Wang, D.-Y. Liu, Physical and chemical properties of sintering red mud and bayer red mud and the implications for beneficial utilization, Materials 5 (2012) 1800–1810, https://doi.org/10.3390/ma5101800.

[6] M.A. Abdelkareem, H.M. Maghrabie, A.G. Abo-Khalil, O.H.K. Adhari, E.T. Sayed, A. Radwan, et al., Battery thermal management systems based on nanofluids for electric vehicles, J. Energy Storage 50 (2022) 104385, https://doi.org/10.1016/j.est.2022.104385.

[7] K. Emara, H. Aliwa, O.E. Abdellatif, H.M. Abd El-hameed, Experimental investigation for a hybrid aluminum oxide nanofluid-phase change material photovoltaic thermal system based on outdoor test conditions, J. Energy Storage 50 (2022) 104261, https://doi.org/10.1016/j.est.2022.104261.

[8] U. Nithiyanantham, A. Zaki, Y. Grosu, L. González-Fernández, A. Anagnostopoulos, M.E. Navarro, et al., Effect of silica nanoparticle size on the stability and thermophysical properties of molten salts based nanofluids for thermal energy storage applications at concentrated solar power plants, J. Energy Storage 51 (2022) 104276, https://doi.org/10.1016/j.est.2022.104276.

[9] H. Adun, M. Adedeji, M. Dagbasi, A. Babatunde, Amelioration of thermodynamic performance and environmental analysis of an integrated solar power generation system with storage capacities using optimized ternary hybrid nanofluids, J. Energy Storage 51 (2022) 104531, https://doi.org/10.1016/j.est.2022.104531.

[10] L. Natrayan, S. Raviteja, V. Swamy Nadh, S. Chidurula, S. Kaliappan, et al., Tanning wastewater strelization in the dark and sunlight using Psidium Guajava Leaf-derived copper oxide nanoparticles and their Characteristics, ACS Omega 8 (42) (2023) 39680–39689, https://doi.org/10.1021/acsomega.3c05588.

[11] A.M. Ajeena, P. Víg, I. Farkas, A comprehensive analysis of nanofluids and their practical applications for flat plate solar collectors: fundamentals, thermophysical properties, stability, and difficulties, Energy Rep. 8 (2022) 4461–4490, https://doi.org/10.1016/j.egyr.2022.03.088.

[12] N. Lakshmaiya, V. Ganesan, P. Paramasivam, S. Dhanasekaran, Influence of biosynthesized nanoparticles addition and fibre content on the mechanical and moisture absorption behaviour of natural fibre composite, Appl. Sci. 12 (24) (2022) 13030, https://doi.org/10.3390/app122413030.

[13] S.N.M. Zainon, W.H. Azmi, Recent progress on stability and thermo-physical properties of mono and hybrid towards green nanofluids, Micromachines 12 (2021) 176, https://doi.org/10.3390/mi12020176.

[14] R. Ranjbarzadeh, A. Moradikazerouni, R. Bakhtiari, A. Asadi, M. Afrand, An experimental study on stability and thermal conductivity of water/silica nanofluid: eco-friendly production of nanoparticles, J. Clean. Prod. 206 (2019) 1089–1100, https://doi.org/10.1016/j.jclepro.2018.09.205.

[15] R. Sadri, K. Zangeneh Kamali, M. Hosseini, N. Zubir, S.N. Kazi, G. Ahmadi, et al., Experimental study on thermo-physical and rheological properties of stable and green reduced graphene oxide nanofluids: hydrothermal assisted technique, J. Dispersion Sci. Technol. 38 (2017) 1302–1310, https://doi.org/10.1080/01932691.2016.1234387.

[16] S.K. Nune, N. Chanda, R. Shukla, K. Katti, R.R. Kulkarni, S. Thilakavathy, et al., Green nanotechnology from tea: phytochemicals in tea as building blocks for production of biocompatible gold nanoparticles, J. Mater. Chem. 19 (2009) 2912, https://doi.org/10.1039/b822015h.

[17] N. L, R. Surakasi, P. Paramasivam, S. Dhanasekaran, K. S, P.P. Patil, Statistical experiment analysis of wear and mechanical behaviour of abaca/sisal fiber-based hybrid composites under liquid nitrogen environment, Front. Mater. 10 (2023) 1218047, https://doi.org/10.3389/fmats.2023.1218047.

[18] M. Bahiraei, S.M. Naghibzadeh, M. Jamshidmofid, Efficacy of an eco-friendly nanofluid in a miniature heat exchanger regarding to arrangement of silver nanoparticles, Energy Convers. Manag. 144 (2017) 224–234, https://doi.org/10.1016/j.enconman.2017.04.076.

[19] R.K. Kotnala, R. Das, J. Shah, S. Sharma, C. Sharma, P.B. Sharma, Red mud industrial waste translated into green electricity production by innovating an ingenious process based on Hydroelectric Cell, J. Environ. Chem. Eng. 10 (2022) 107299, https://doi.org/10.1016/j.jece.2022.107299.

[20] P. Kanti, K.V. Sharma, K.M. Yashawantha, S. Dmk, Experimental determination for viscosity of fly ash nanofluid and fly ash-Cu hybrid nanofluid:Prediction and optimization using artificial intelligent techniques, Energy Sources, Part A Recovery, Util. Environ. Eff. (2021) 1–20, https://doi.org/10.1080/15567036.2021.1877374.

[21] P. Kanti, K.V. Sharma, G.R. C, W.H. Azmi, Experimental determination of thermophysical properties of Indonesian fly-ash nanofluid for heat transfer applications, Part. Sci. Technol. 39 (2021) 597–606, https://doi.org/10.1080/02726351.2020.1806971.

[22] P.K. Kanti, K.V. Sharma, Z. Said, M. Gupta, Experimental investigation on thermo-hydraulic performance of water-based fly ash–Cu hybrid nanofluid flow in a pipe at various inlet fluid temperatures, Int. Commun. Heat Mass Tran. 124 (2021) 105238, https://doi.org/10.1016/J.ICHEATMASSTRANSFER.2021.105238.

[23] A. Sözen, H.İ. Variyenli, M.B. Özdemir, M. Gürü, Improving the thermal performance of parallel and cross-flow concentric tube heat exchangers using fly-ash nanofluid, Heat Tran. Eng. 37 (2016) 805–813, https://doi.org/10.1080/01457632.2015.1080574.

[24] B. Palaniappan, V. Ramasamy, Thermodynamic analysis of fly ash nanofluid for automobile (heavy vehicle) radiators, J. Therm. Anal. Calorim. 136 (2019) 223–233, https://doi.org/10.1007/s10973-018-7844-0.

[25] H.I. Variyenli, Experimental and numerical investigation of heat transfer enhancement in a plate heat exchanger using a fly ash nanofluid, Heat Tran. Res. 50 (2019) 1477–1494, https://doi.org/10.1615/HeatTransRes.2019029136.

[26] A.G.N. Sofiah, M. Samykano, A.K. Pandey, K. Kadirgama, K. Sharma, R. Saidur, Immense impact from small particles: review on stability and thermophysical properties of nanofluids, Sustain. Energy Technol. Assessments 48 (2021) 101635, https://doi.org/10.1016/j.seta.2021.101635.

[27] F. Rubbi, K. Habib, R. Saidur, N. Aslfattahi, S.M. Yahya, L. Das, Performance optimization of a hybrid PV/T solar system using Soybean oil/MXene nanofluids as A new class of heat transfer fluids, Sol. Energy 208 (2020) 124–138, https://doi.org/10.1016/j.solener.2020.07.060.

[28] N. Aslfattahi, L. Samylingam, A.S. Abdelrazik, A. Arifutzzaman, R. Saidur, MXene based new class of silicone oil nanofluids for the performance improvement of concentrated photovoltaic thermal collector, Sol. Energy Mater. Sol. Cell. 211 (2020) 110526, https://doi.org/10.1016/j.solmat.2020.110526.

[29] N. Abdullah, R. Saidur, A.M. Zainoodin, N. Aslfattahi, Optimization of electrocatalyst performance of platinum–ruthenium induced with MXene by response surface methodology for clean energy application, J. Clean. Prod. 277 (2020) 123395, https://doi.org/10.1016/j.jclepro.2020.123395.

[30] P. Equipment, ASHRAE Handbook — Fundamentals ASHRAE Handbook — Refrigeration, SI Edition, Refrigerating andAir-Conditioning Engineers, Inc, Atlanta, 2020.

[31] E.C. Okonkwo, I. Wole-Osho, D. Kavaz, M. Abid, Comparison of experimental and theoretical methods of obtaining the thermal properties of alumina/iron mono and hybrid nanofluids, J. Mol. Liq. 292 (2019) 111377, https://doi.org/10.1016/j.molliq.2019.111377.

[32] A. Asadi, M. Asadi, A. Rezaniakolaei, L.A. Rosendahl, M. Afrand, S. Wongwises, Heat transfer efficiency of Al2O3-MWCNT/thermal oil hybrid nanofluid as a

cooling fluid in thermal and energy management applications: an experimental and theoretical investigation, Int. J. Heat Mass Tran. 117 (2018) 474–486, https://doi.org/10.1016/j.ijheatmasstransfer.2017.10.036.
[33] V. Kumar, A. Pare, A.K. Tiwari, S.K. Ghosh, Efficacy evaluation of oxide-MWCNT water hybrid nanofluids: an experimental and artificial neural network approach, Colloids Surf. A Physicochem. Eng. Asp. 620 (2021) 126562, https://doi.org/10.1016/j.colsurfa.2021.126562.
[34] S.R. Nfawa, A.R. Abu Talib, A.A. Basri, S.U. Masuri, Novel use of MgO nanoparticle additive for enhancing the thermal conductivity of CuO/water nanofluid, Case Stud. Therm. Eng. 27 (2021) 101279, https://doi.org/10.1016/j.csite.2021.101279.
[35] A. Hosseinzadeh, J.L. Zhou, A. Altaee, D. Li, Machine learning modeling and analysis of biohydrogen production from wastewater by dark fermentation process, Bioresour. Technol. 343 (2022) 126111, https://doi.org/10.1016/j.biortech.2021.126111.
[36] M. Jamei, M. Karbasi, I. Adewale Olumegbon, M. Mosharaf-Dehkordi, I. Ahmadianfar, A. Asadi, Specific heat capacity of molten salt-based nanofluids in solar thermal applications: a paradigm of two modern ensemble machine learning methods, J. Mol. Liq. 335 (2021) 116434, https://doi.org/10.1016/j.molliq.2021.116434.
[37] S. Wan, X. Li, Y. Yin, J. Hong, Milling chatter detection by multi-feature fusion and Adaboost-SVM, Mech. Syst. Signal Process. 156 (2021) 107671, https://doi.org/10.1016/j.ymssp.2021.107671.
[38] W. Wang, D. Sun, The improved AdaBoost algorithms for imbalanced data classification, Inf Sci (N Y) 563 (2021) 358–374, https://doi.org/10.1016/j.ins.2021.03.042.
[39] W. Wang, D. Sun, The improved AdaBoost algorithms for imbalanced data classification, Inf Sci (N Y) 563 (2021) 358–374, https://doi.org/10.1016/J.INS.2021.03.042.
[40] L. Zhou, D. Garg, Y. Qiu, S.M. Kim, I. Mudawar, C.R. Kharangate, Machine learning algorithms to predict flow condensation heat transfer coefficient in mini/micro-channel utilizing universal data, Int. J. Heat Mass Tran. 162 (2020) 120351, https://doi.org/10.1016/j.ijheatmasstransfer.2020.120351.
[41] L. Guelman, Gradient boosting trees for auto insurance loss cost modeling and prediction, Expert Syst. Appl. 39 (2012) 3659–3667, https://doi.org/10.1016/j.eswa.2011.09.058.
[42] I. Jebli, F.-Z. Belouadha, M.I. Kabbaj, A. Tilioua, Prediction of solar energy guided by pearson correlation using machine learning, Energy 224 (2021) 120109, https://doi.org/10.1016/j.energy.2021.120109.
[43] J.P. de Amorim Neto, F.P. Marinho, R.J.P. Lima, P.A.C. Rocha, S.P. Mendonça, A.V. Bueno, et al., Thermal behavior estimation of a solar wall operated by TiO2 nanofluids using several machine learning models, J. Braz. Soc. Mech. Sci. Eng. 44 (2022) 128, https://doi.org/10.1007/s40430-022-03425-x.
[44] M. Jamei, I. Ahmadianfar, A rigorous model for prediction of viscosity of oil-based hybrid nanofluids, Phys. Stat. Mech. Appl. 556 (2020) 124827, https://doi.org/10.1016/j.physa.2020.124827.
[45] Z. Said, P. Sharma, N. Aslfattahi, M. Ghodbane, Experimental analysis of novel ionic liquid-MXene hybrid nanofluid's energy storage properties: model-prediction using modern ensemble machine learning methods, J. Energy Storage 52 (2022) 104858, https://doi.org/10.1016/j.est.2022.104858.
[46] M. Awais, A.A. Bhuiyan, S. Salehin, M.M. Ehsan, B. Khan, MdH. Rahman, Synthesis, heat transport mechanisms and thermophysical properties of nanofluids: a critical overview, International Journal of Thermofluids 10 (2021) 100086, https://doi.org/10.1016/j.ijft.2021.100086.
[47] A.K. Tiwari, N.S. Pandya, H. Shah, Z. Said, Experimental comparison of specific heat capacity of three different metal oxides with MWCNT/water-based hybrid nanofluids: proposing a new correlation, Appl. Nanosci. (2020), https://doi.org/10.1007/s13204-020-01578-6.
[48] P. Kanti, K.V. Sharma, R.S. Khedkar, T. Rehman, Synthesis, characterization, stability, and thermal properties of graphene oxide based hybrid nanofluids for thermal applications: experimental approach, Diam. Relat. Mater. 128 (2022) 109265, https://doi.org/10.1016/j.diamond.2022.109265.
[49] R. Prasher, D. Song, J. Wang, P. Phelan, Measurements of nanofluid viscosity and its implications for thermal applications, Appl. Phys. Lett. 89 (2006) 133108, https://doi.org/10.1063/1.2356113.
[50] Z. Said, P. Sharma, N. Aslfattahi, M. Ghodbane, Experimental analysis of novel ionic liquid-MXene hybrid nanofluid's energy storage properties: model-prediction using modern ensemble machine learning methods, J. Energy Storage 52 (2022) 104858, https://doi.org/10.1016/j.est.2022.104858.
[51] P. Kanti, K.V. Sharma, Y. Raja Sekhar, Influence of particle size on thermal conductivity and dynamic viscosity of water-based Indian coal fly ash nanofluid, Heat Transfer 51 (2022) 413–433, https://doi.org/10.1002/htj.22313.
[52] B.C. Pak, Y.I. Cho, Hydrodynamic and heat transfer study of dispersed fluids with submicron metallic oxide particles, Exp. Heat Tran. 11 (1998) 151–170, https://doi.org/10.1080/08916159808946559.

Update

Case Studies in Thermal Engineering

Volume 55, Issue , March 2024, Page

DOI: https://doi.org/10.1016/j.csite.2024.104155

Case Studies in Thermal Engineering 55 (2024) 104155

Contents lists available at ScienceDirect

Case Studies in Thermal Engineering

journal homepage: www.elsevier.com/locate/csite

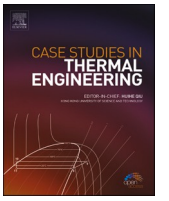

Corrigendum to "Artificial intelligence-assisted characterization and optimization of red mud-based nanofluids for high-efficiency direct solar thermal absorption" [Case Stud. Therm. Eng. 54, (February 2024), 104087]

K. Praveen Kumar [a], Rohit Khedkar [b], Prabhakar Sharma [c], Rajvikram Madurai Elavarasan [d], Prabhu Paramasivam [e], V. Vicki Wanatasanappan [a], Sesathiri Dhanasekaran [f,*]

[a] *Institute of Power Engineering, Universiti Tenaga Nasional, Jalan IKRAM-UNITEN, 43000, Selangor, Malaysia*
[b] *Department of Chemical Engineering, School of Engineering, P P Savani University, Surat, 395009, Gujarat, India*
[c] *Department of Mechanical Engineering, Delhi Skill and Entrepreneurship University, Delhi, 110089, India*
[d] *Research and Development Division, Nestlives Private Limited, Chennai, 600091, India*
[e] *Department of Research and Innovation, Saveetha School of Engineering, SIMATS, Chennai, Tamilnadu, 602105, India*
[f] *Department of Computer Science, UiT The Arctic University of Norway, Tromso, Norway*

The authors regret the incorrect inclusion of the acknowledgment section in the article. We request that you remove the acknowledgment section from our paper.

The authors would like to apologize for any inconvenience caused.

DOI of original article: https://doi.org/10.1016/j.csite.2024.104087.
* Corresponding author.
E-mail address: Seshathiri.dhanasekaran@uit.no (S. Dhanasekaran).

https://doi.org/10.1016/j.csite.2024.104155

Available online 19 February 2024